aerospace

MDPI

Article

Effective Distance for Vortex Generators in High Subsonic Flows

Ping-Han Chung [1], Yi-Xuan Huang [2], Kung-Ming Chung [1,*], Chih-Yung Huang [3] and Sergey Isaev [4]

[1] Aerospace Science and Technology Research Center, National Cheng Kung University, Tainan 711, Taiwan
[2] Department of Aeronautics and Astronautics, National Cheng Kung University, Tainan 701, Taiwan
[3] Department of Power Mechanical Engineering, National Tsing Hua University, Hsinchu 300, Taiwan
[4] Basic Research Laboratory, St. Petersburg State University of Civil Aviation, 38 Pilotov Street, St. Petersburg 196210, Russia
* Correspondence: kmchung@mail.ncku.edu.tw; Tel.: +886-6-239281

Abstract: Vortex generators (VGs) are a passive method by which to alleviate boundary layer separation (BLS). The device-induced streamwise vortices propagate downstream. There is then lift-off from the surface and the vortex decays. The effectiveness of VGs depends on their geometrical configuration, spacing, and flow characteristics. In a high-speed flow regime, the VGs must be properly positioned upstream of the BLS region. Measurements using discrete pressure taps and pressure-sensitive paint (PSP) show that there is an increase in the upstream surface pressure and the downstream favorable pressure gradient. The effective distance for a flat plate in the presence of three VG configurations is determined, as is the height of the device (conventional and micro VGs).

Keywords: effective distance; vortex generator; pressure-sensitive paint; high subsonic flow

Citation: Chung, P.-H.; Huang, Y.-X.; Chung, K.-M.; Huang, C.-Y.; Isaev, S. Effective Distance for Vortex Generators in High Subsonic Flows. *Aerospace* **2023**, *10*, 369. https://doi.org/10.3390/aerospace10040369

Academic Editor: Zhenbing Luo

Received: 6 February 2023
Revised: 16 March 2023
Accepted: 10 April 2023
Published: 12 April 2023

1. Introduction

Boundary layer separation (BLS) results in increased drag and total-pressure losses, which reduces the aerodynamic efficiency of flight vehicles [1]. Ashill et al. [2] showed that BLS can be prevented by increasing the magnitude of the vorticity near the wall: decreasing the imposed adverse pressure gradient (body shaping), removing the low-momentum near-wall flow (suction), adding momentum to the near-wall flow (blowing or jet), and increasing the mixing between the high-energy layers in the outer part of the boundary layer and the low energy regions near the walls (VGs). Active flow control techniques (suction or blowing) are effective, but require an external energy input. Passive control devices (VGs) feature simple construction, but the optimal configuration to mitigate BLS in both external and internal aerodynamics is yet to be determined.

BLS results in large energy losses. The presence of VGs increases the near-wall momentum because the momentum is transferred from the outer flow to the wall region [3], so the separation region is reduced or eliminated. The flow structure for a VG with counter-rotating vanes (CRV), which induce two opposite vortices, is shown in Figure 1. This transfer of momentum results in a fuller boundary layer profile, which is more resistant to an adverse pressure gradient [4–6]. A VG of a height, h, is the same order of the thickness as the incoming boundary layer, δ, (a conventional VG) or less (h/δ or $h^* < 1$). A device at an angle of incidence, α, to the local flow is typically normal to the surface and produces an array of streamwise trailing vortices. The strength of these vortices and the decay downstream depend on the configuration of VGs (shape, h/δ, spacing). The effectiveness of VGs is also associated with flow characteristics (the state of the boundary layer, freestream Mach number M, and Reynolds number). Titchner and Babinsky [7] showed that the presence of VGs is more effective at transonic conditions and shock-induced separation has been markedly reduced. However, it is not true for pure supersonic cases, which is not as

consistent in low-speed applications. In a transonic flow regime, the best performance is achieved with $h^* \approx 0.5$ and a shape similar to a swept vane.

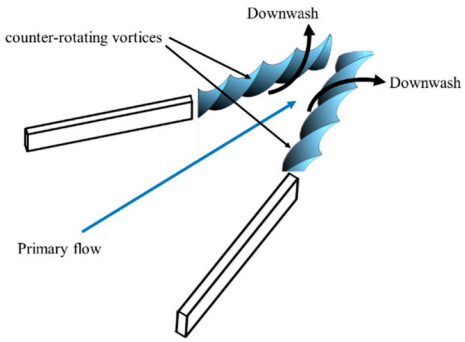

Figure 1. Flow structure of a counter-rotating VG with counter-rotating vanes.

A common VG comprises rectangular thin-plate vanes. CRV VGs produce a stronger vortex downstream of the device than that of VGs with co-rotating vanes (CoV) [8] and have a uniform effect on the boundary layer flow. Ramp (or wedge) VGs are structurally robust and are eminently suited to applications in high-speed flows [9]. Leading edge separation produces a pair of weak trailing vortices. A strong primary vortex pair is shed from the slant top edges of a Ramp VG [10,11]. The vortex strength of a CRV VG is about twice as strong as that from a Ramp VG [3,12]. There are early lift-off vortices for a Ramp VG, which are less effective than a CRV or a CoV VG [13].

The ratio h^* ($=h/\delta$) has the greatest effect on the effectiveness of VGs. A conventional VG generates vortices that are sustained farther downstream. However, the device-induced drag is greater. This partially mitigates the benefits. A sub-δ or micro VG (MVG) produces similar mixing levels and creates less device drag than a conventional VG. There is a decrease in the vortex strength for a MVG and the effective distance, L, decreases as h^* decreases [14].

The spacing of adjacent VGs, D, is another important factor in establishing an effective vortex pattern. The VG-induced vortices exert a greater effect on the boundary layer near the surface. Pearcey [15] showed that the centers of the vortices move closer together in pairs and further away from the surface. There is mutual vortex damping because adjacent vortices are close. This is particularly true for the interaction between two opposite vortices that are created by CRV VGs and the vortex decays faster. A minimum value ($D \approx 3\,h$) is required to establish an effective vortex pattern over a region of several h.

VGs are positioned upstream of a region with adverse flow conditions. These create vortices that persist downstream and allow momentum transfer toward the wall. The rate of decay of the vortices determines the streamwise extent of the device. Pearcey [15] reported that the VG-induced streamwise vortices can be sustained up to 100 h. The streamwise range of effectiveness for VGs increases as h^* increases, so a decrease in h^* results in a decrease in L. MVGs must be placed closer to the location of separation because VGs have limited effectiveness downstream. The value of L for MVGs is about 5–30 h ($M = 0.2$) [3] or the order of 10 δ (low-speed flow) [2].

Ashill et al. [2] showed that the strength of a vortex just downstream of a VG is directly proportional to the value of M and VGs must be properly positioned upstream of the separation region. Chung et al. [16] determined the effect of VGs upstream of a convex corner to mitigate BLS. The trailing edge for VGs was located at 0.43 δ from the corner apex. For a convex-corner angle of 13° and 15°, the respective separation locations for $M = 0.83$ are 2.8–3.1 δ downstream of the corner, which is 5.9–8.0 δ for $M = 0.89$. The data for the study shows that VGs are less effective for $M = 0.89$. This corresponds to the effectiveness for VGs because of the distance between VGs and the separation region.

The position for VGs has a significant effect on the control of BLS, but data is scarce in the literature. This study installs VGs (CRV, CoV, and Ramp) on a flat plate and determines

surface pressure distribution (a Kulite pressure sensor and PSP). A region of downstream favorable pressure gradient in the presence of the VGs is determined. In this context, the VG-induced vortical structure and thermal quenching effect for the PSP technique are considered. The region of effective vortex in the presence of VGs (or L) is determined, in which there is the agreement between the PSP (thermal quenching effect) and Kulite measurements. The effect of h^* (=0.2, 0.5 and 1.0) and the type of VG (CRV, CoV, and Ramp) on the value of L in high subsonic flows (M = 0.64 and 0.83) is determined. Before discussing the results, details of the experiment setup are outlined.

2. Experimental Setup

2.1. Transonic Wind Tunnel

This experiment was conducted in a transonic wind tunnel (blowdown type) at the Aerospace Science and Technology Research Center of National Cheng Kung University (ASTRC/NCKU). The high-pressure supply system consists of two compressors, two air dryers (dew point ≈ -40 °C), a cooling water system, and three air storage tanks (a total volume of 180 m^3 with the maximum pressure of 50 bars). A rotary perforated sleeve valve controls the stagnation pressure, p_o. High-pressure air is discharged into a stilling chamber through flow spreaders. Inside the stilling chamber, acoustic baffles, three screens, and a honeycomb absorb control valve noise and reduce the intensity of freestream turbulence. The constant-area test section, which is assembled using solid sidewalls and perforated top/bottom walls (6% porosity), has a cross-sectional area of 600 mm $\times$ 600 mm and a length of 1500 mm. The operational Mach number ranges from 0.2 to 1.4. The unit Reynolds number has a maximum value of 2×10^7/m. The centerline Mach number uniformity for the test section is 0.005. The value of p_o is 172 $\pm$ 0.5 kPa and the stagnation temperature is 28–32 °C for this study. The test conditions are monitored and recorded using a National Instruments system (PXIe-8840 RT, PXI-7846, PXI-6511, and PXI-6513; Austin, TX, USA).

2.2. Test Model

The test model is a flat plate and an instrumentation plate with an array of VGs, as shown in Figure 2. The flat plate has a 450-mm long flat plate with a leading edge of 3° to ensure that a turbulent boundary layer naturally develops and a 180-mm instrumentation plate with VGs. For surface pressure measurements using Kulite sensors and the PSP technique, there are nine interchangeable instrumentation plates with different VG configurations (CRV, CoV, and Ramp types; h^* = 0.2, 0.5, and 1.0). The values of M are 0.64 and 0.83 $\pm$ 0.01 and the respective value of δ at 475 mm from the leading edge is 7.3 and 7.1 $\pm$ 0.2 mm [17]. If uncertainty is considered, the value of δ is approximately 7 mm for both Mach numbers. The normalized boundary layer profiles, as shown in Figure 3 ($n \approx$ 7–11 for the velocity power law), are determined using a Pitot probe and a transversing device. The respective Reynolds numbers based on δ, Re_δ, are 1.63 and 1.69 $\times$ 10^5.

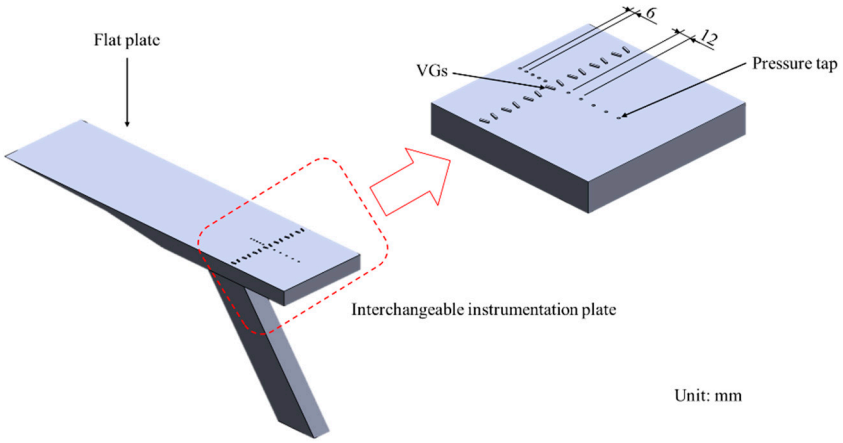

Figure 2. Test configuration.

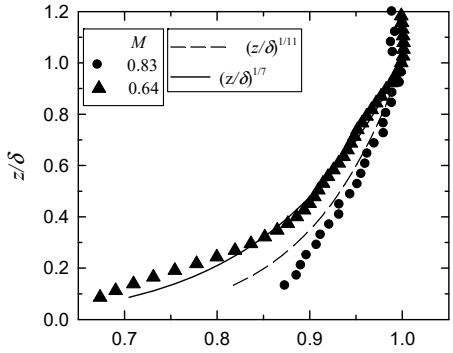

Figure 3. Normalized velocity profiles for M = 0.64 and 0.83.

Ten pressure taps (2.5-mm in diameter) were machined perpendicular to the surface of each instrumentation plate along the centerline. Five pressure taps were upstream (spacing = 6 mm) and five were downstream (spacing = 12 mm) of the VGs, respectively, as shown in Figure 2. Three types of VGs (CRV, CoV, and Ramp) were used [16]. Sketches of the VGs are shown in Figure 4 and the parameters are listed in Table 1. All VGs had a length, l, of 1 δ and a value for α of 15°. The width of the CRV and CoV types, w_v, was 0.2 δ and, for the Ramp type, w_r, it was 0.5 δ. Pearcey [15] determined that there is increased mixing at the inner edge of the boundary layer as spacing increases. The spacing, D, between VGs was 3 δ (or D/h = 3–15) in order to establish an effective vortex pattern ($D/h \geq 3$). An array of seven VGs was created. For the CRV type, the front, d, and rear, s, spacing are 1 δ and 0.5 δ, respectively.

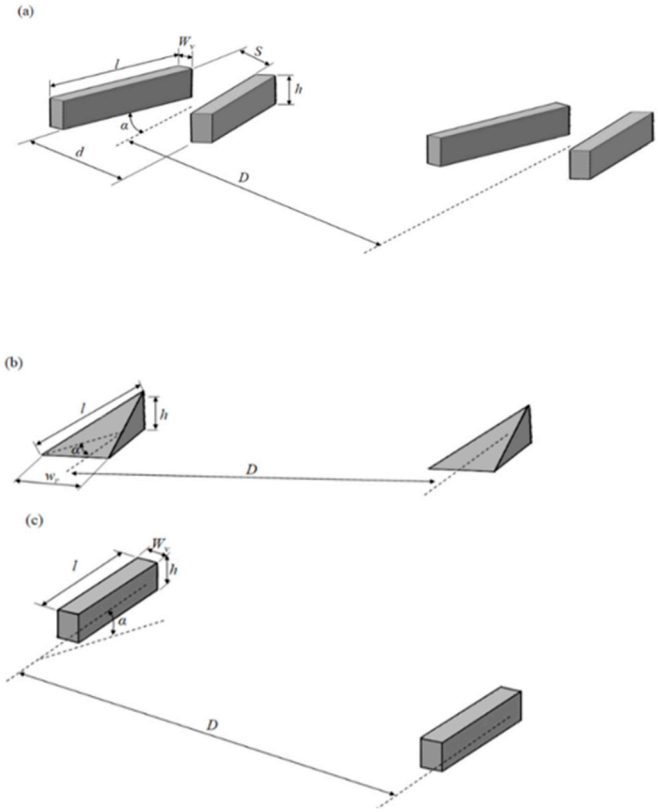

Figure 4. Configuration of VGs: (**a**) CRV type, (**b**) Ramp type, and (**c**) CoV type [16].

Table 1. Geometry of the VGs.

Parameters	Value
h/δ	0.2, 0.5, 1.0
l/δ	1.0
D/δ	3.0
w_v/δ	0.2
w_r/δ	0.5
s/δ	0.5
d/δ	1.0
α	15°

2.3. Instrumentation and Data Acquisition System

Mean surface pressure was measured using flush-mounted Kulite pressure transducers (Model XCS-093-25A, B screen; Leonia, NJ, USA). The nominal outer diameter of the sensors is 2.36 mm. The pressure sensors were powered by a DC power supply (GW Instek PSS-3203; Taipei, Taiwan) of 10.0 V and external amplifiers (Ectron Model 753A; San Diego, CA, USA) were used to increase the signal-to-noise ratio. A National Instruments (CI SCXI; Austin, TX, USA) device triggered all input channels and recorded data. The sampling rate was 5 µs. Each measurement consisted of 131,072 data points. The uncertainty in the mean surface pressure coefficient, C_p ($=\frac{p-p_\infty}{q}$) is 0.43%, where p_∞ is the freestream static pressure and q is the dynamic pressure.

The PSP technique has been used to determine the pattern of the global surface pressure [18–21]. A schematic drawing of the measurement system is shown in Figure 5. The UniFIB PSP was purchased from ISSI Co. (Dayton, OH, USA). It is a blend of Fluoro/Isopropyl/Butyl polymer (FIB), Platinum tetra (pentafluorophyenyl) porphine (Pt-TFPP), and white pigment. The absorption and emission spectra are 380–520 nm and 620–750 nm, respectively. The response time that is quoted by the manufacturer is 300 ms. The PSP-coated surface was illuminated using two excitation light-emitting diode (LED) light sources (Revox SLG-55, Kanagawa, Japan) with a 550-nm short-pass optical filter, and the emitted signal was captured using a Charge Coupled Device (CCD) camera (PCO Pixelfly, Regensburg, Germany; 1392 × 1040 pixels; 1 pixel ≈ 0.21 mm; sampling rate = 20 frame/s) with a 600-nm long-pass optical filter. The Stern-Volmer equation shows that the intensity of the emission is inversely proportional to the local surface pressure on the test model as [22]:

$$\frac{I\left(p_{ref}, T_{ref}\right)}{I(p,T)} = A(T) + B(T)\frac{p}{p_{ref}}$$

where $A(T)$ and $B(T)$ are temperature-dependent coefficients.

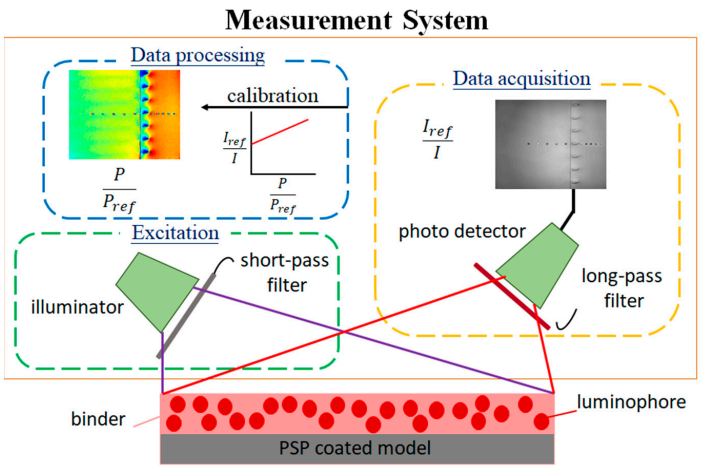

Figure 5. PSP measurement system.

Figure 6 shows the calibration curve using 32 images, in which the applied pressure varied from 1.0 to 1.44 bar. There is a linear relationship between the intensity ratio for the luminescence, I_{ref}/I, and the pressure ratio, p/p_{ref}, where I_{ref} and p_{ref} are the reference intensity and pressure, respectively. The value for $B(T)$, which is the pressure sensitivity, is 0.66%/kPa. Thermal quenching results in a temperature sensitivity of −0.4%/°C. For the wind tunnel test, the I_{ref} was recorded by taking the wind-off images that were immediately captured after the wind tunnel was shut down. A median filter function (removing noise from an image) in the Matlab program was used to transform the luminescent intensity to surface pressure using the calibration curve [23].

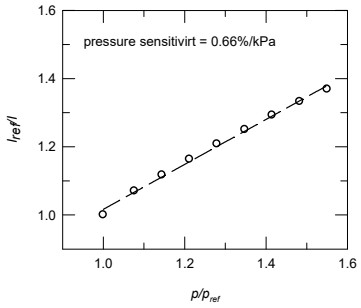

Figure 6. The calibration curve for UniFIB PSP.

3. Results and Discussion

3.1. Surface Pressure Pattern

Examples of the global C_p pattern for a flat plate in the presence of VGs are shown in Figures 7 and 8. For M = 0.64 and h^* = 1.0, CRV VGs produce a stronger vortex (lower pressure). The vortex for CRV VGs decays faster than that for CoV and Ramp VGs. This is because of the interaction between two opposite vortices. For an airfoil, VGs are typically positioned on the upper surface to mitigate BLS. An increase in the value of C_p upstream of the VGs represents greater device-induced drag and a reduction in lift, which mitigates the benefits. The induced vortex is weakest for Ramp VGs. For M = 0.83, the effect of the VG configuration on the global surface pressure pattern is similar to that for M = 0.64. There is a stronger induced vortex near the VGs as M increases.

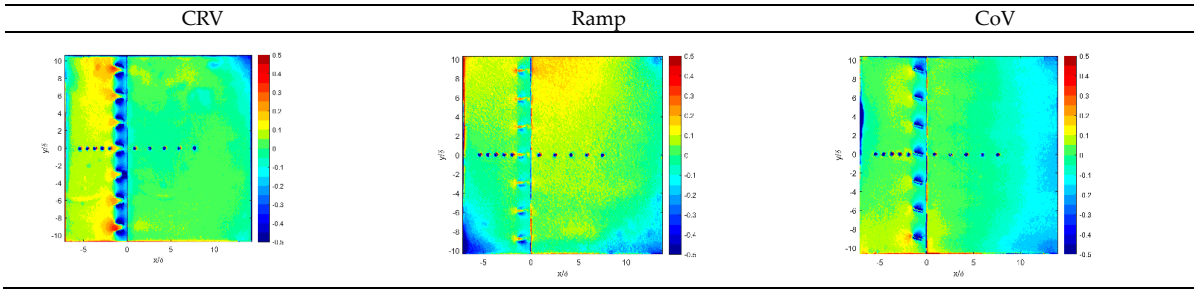

Figure 7. Global surface pressure pattern for M = 0.64 and h^* = 1.0.

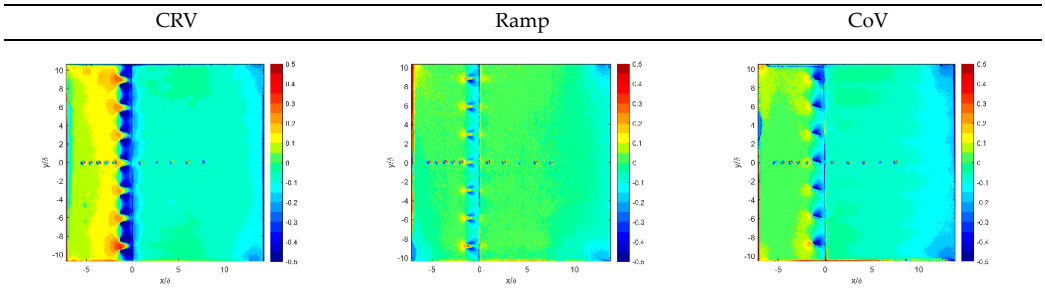

Figure 8. Global surface pressure pattern for M = 0.83 and h^* = 1.0.

The C_p distributions (h^* = 0.2, 0.5, and 1.0) for M = 0.83 and y^* = 0 that were measured using Kulite sensors and the PSP technique are shown in Figure 9. The horizontal axis is the normalized streamwise location, x^* (=x/δ), and the origin is 3 mm downstream of the trailing edge of the VGs. There is a good agreement between two measurement techniques upstream of the CoV VGs. An increase in the value of C_p represents a decrease in lift (performance penalty). The discrepancy downstream of the VGs is associated with thermal quenching using the PSP technique. More details are given in the following section. The downstream favorable pressure gradient is created by device-induced streamwise co-rotating vortices.

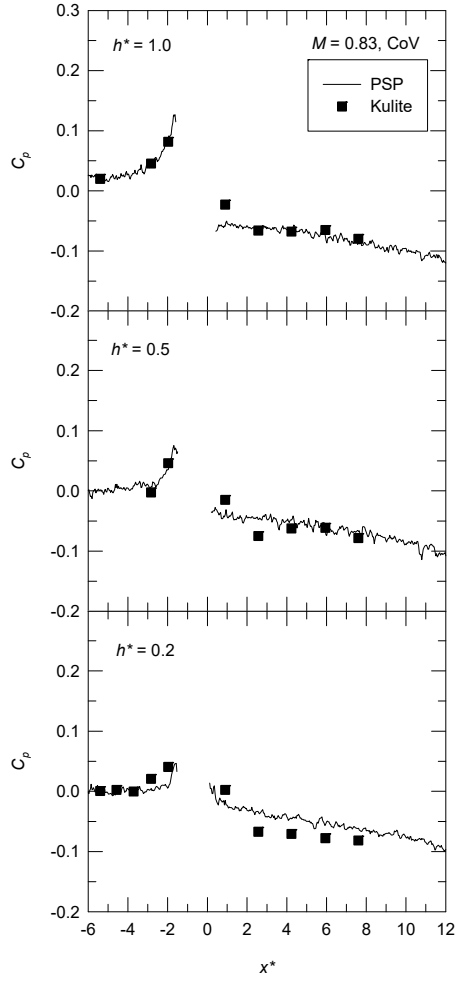

Figure 9. The effect of CoV VG on the centerline surface pressure distribution for M = 0.83.

The drag penalty for VGs is defined in terms of the upstream peak mean surface pressure, $C_{p,max}$. The data for M = 0.64 and 0.83 are shown in Figure 10. The Kulite measurements (solid symbols) show that for CRV and CoV VGs, there is an increase in the value of $C_{p,max}$ as h^* increases, but not for Ramp VGs. This is due to the spatial resolution of the discrete pressure taps. The PSP data (hollow symbols) show the effect of h^* on the value of $C_{p,max}$. Conventional VGs (h^* = 1.0) result in an increase in value of $C_{p,max}$ more significantly than MVGs (h^* = 0.2 and 0.5). The effect is particularly noticeable for CRV and Ramp VGs. This is a factor in quantifying the overall performance of VGs for BLS control.

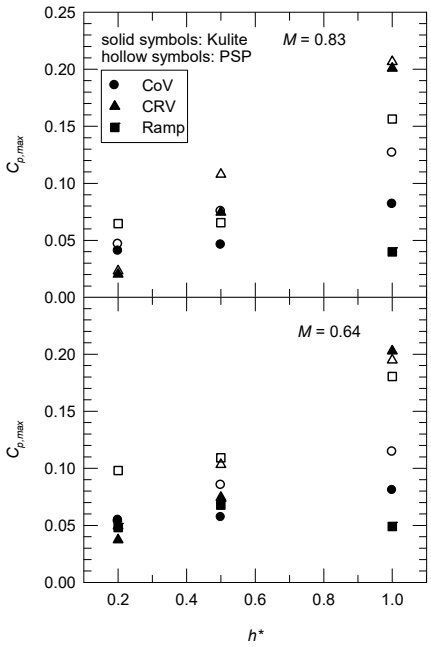

Figure 10. The maximum surface pressure coefficient upstream of the VGs.

3.2. Effective Distance

As shown in Figure 9, VGs create a region of downstream favorable pressure gradient. For $h^* = 1.0$, the distribution of C_p in the presence of CoV VGs at $y^* = 0$ is shown in Figure 11. The pressure measurements using Kulite sensors show that the value of C_p for $M = 0.64$ and 0.83 is approximately the same upstream of the VGs. There is a greater downstream favorable pressure gradient for $M = 0.83$ because the vortex is stronger. A mild variation in the value of C_p at farther downstream locations is determined.

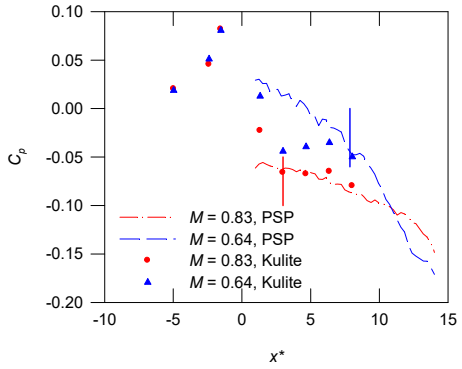

Figure 11. Pressure distribution in the presence of CoV VGs for $h^* = 1.0$.

The PSP data is not consistent with that for the Kulite sensors within a region of several δ because the vortical structure downstream of the CoV VGs is stronger, as is the thermal quenching effect for the PSP measurements [19]. For $M = 0.83$, the PSP data approaches the Kulite measurements more quickly. If the VG-induced vortical structure and thermal quenching effect for the PSP measurements are considered, the region of effective vortex in the presence of VGs (or L) extends to the location where there is agreement between the PSP and Kulite measurements, which is shown as the vertical lines in Figure 11.

The downstream favorable pressure gradient depends on the strength of the VG-induced vortices. The measurements used Kulite sensors, as shown in Figure 12. For MVGs ($h^* \leq 0.5$), CoV VGs produce a greater pressure gradient downstream of the device than CRV and Ramp VGs. The value of the favorable pressure gradient decreases as h^* increases for CRV and Ramp VGs, but not for CoV VGs. This phenomenon is more significant for

M = 0.83. For a conventional VG, counter-rotating vortices (CRV and Ramp VGs) induce a greater favorable pressure gradient and there is less difference between the results for different VG configurations.

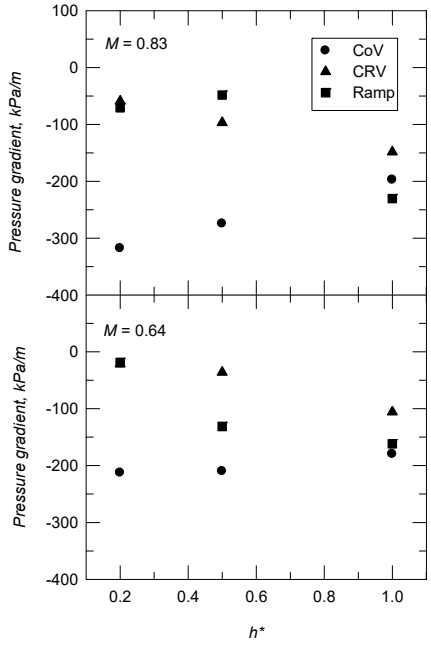

Figure 12. Downstream pressure gradient.

The effectiveness of VGs depends on their location upstream of the region to be controlled. The value of L is normalized by δ ($L^* = L/\delta$), as shown in Figure 13. For M = 0.83, L^* ranges from 3.0 to 8.4. The effect of VG configuration varies. For CoV VGs, there is a decrease in L^* as h^* increases. This is consistent with the effect of h^* on the downstream favorable pressure gradient, as shown in Figure 11. The value for L^* (=8.4) for Ramp VGs is a maximum for h^* = 0.5. The value of h^* has a slight effect on L^* for CRV VGs. For M = 0.64, the effect of h^* on L^* is less significant for all three VG configurations. The device-induced vortices in the presence of CoV VGs extend for a longer distance.

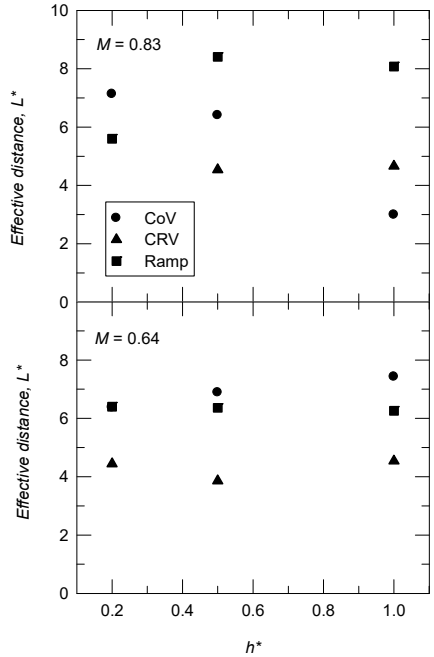

Figure 13. Effective distance, L/δ.

The effective distance is also scaled by the device height. The ratio between L and h is shown in Figure 14. The value of L/h ranges from 3 to 36, which is in agreement with the results by the study by Lin (L/h = 5–30) [3]. There is a decrease in the value of L/h as h^* increases for M = 0.83 and 0.64, and the effect of M is less significant.

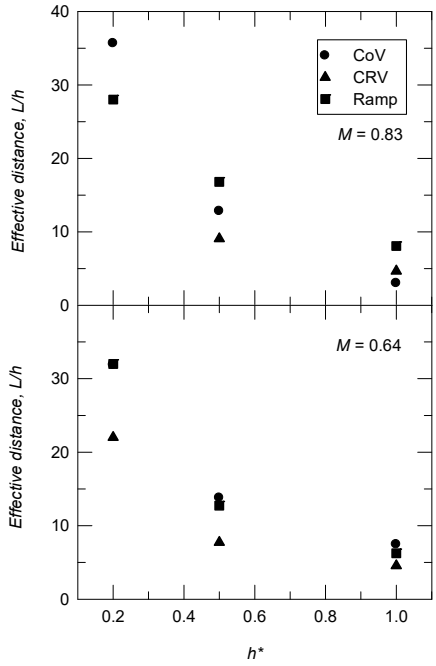

Figure 14. Effective distance, L/h.

4. Conclusions

Vortex generators are used to alleviate boundary layer separation. Their effectiveness depends on the geometrical configuration and the device height. The position of vortex generators upstream of the separation region is also an important factor. Surface pressure measurements using discrete pressure taps (Kulite sensors) and pressure-sensitive paint determine the upstream influence (performance penalty) and the downstream favorable pressure gradient (footprint of streamwise vortical structure) for M = 0.64 and 0.83.

Vortex generators should be properly positioned upstream of the region of boundary layer separation. The presence of vortex generators results in an increase in the value of upstream surface pressure. The increase is more significant for conventional vortex generators (h^* = 1.0) than for micro vortex generators (h^* = 0.2 and 0.5), particularly for vortex generators using counter-rotating vanes or ramp (device-induced counter-rotating vortices). This determines a greater device-induced drag and a reduction in lift using conventional vortex generators. Micro co-rotating vortex generators produce a greater streamwise favorable pressure gradient downstream of the device than micro counter-rotating and ramp vortex generators. The effect of h^* (conventional vortex generators or micro vortex generators) is greater for vortex generators using counter-rotating vanes or ramp, but not for vortex generators using co-rotating vanes. The value of L depends on the configuration of vortex generator, M, and h^*. The value ranges from 3.0 to 8.4 δ (or 3–36 h) and there is a decrease in the value of L/h as h^* increases. The data for this study can be used to position vortex generators in high subsonic flows to ensure more effective control for boundary layer separation.

Author Contributions: Conceptualization, K.-M.C., C.-Y.H. and S.I.; methodology, P.-H.C., Y.-X.H., C.-Y.H. and S.I.; formal analysis, P.-H.C.; data curation, P.-H.C. and Y.-X.H.; writing—original draft preparation, P.-H.C.; writing—review and editing, K.-M.C., C.-Y.H. and S.I.; funding acquisition, K.-M.C., C.-Y.H. and S.I. All authors have read and agreed to the published version of the manuscript.

Funding: This study was funded by the National Science and Technology Council, Taiwan; grant number MOST 107-2212-E-006-115-MY3.

Data Availability Statement: Data is available upon request.

Acknowledgments: The authors are grateful for the technical support of the ASTRC/NCKU technical staff.

Conflicts of Interest: The authors declare no conflict of interest.

Nomenclature

$A(T)$	constant for PSP calibration curve
$B(T)$	pressure sensitivity
C_p	surface pressure coefficient
$C_{p,max}$	peak surface pressure coefficient upstream of vortex generator
d	front spacing of counter-rotating vortex generator
D	spacing between adjacent vortex generators
h	height of vortex generator
I	intensity of the emission
I_{ref}	reference intensity of emission
h^*	normalized height of vortex generator, h/δ
l	length of vortex generator
L	effective distance
L^*	normalized effective distance, L/δ
M	freestream Mach number
p_o	stagnation pressure
p_{ref}	reference pressure (= ambient pressure)
q	dynamic pressure
s	rear spacing of counter-rotating vortex generator
T	temperature
u	velocity
U_∞	freestream velocity
w	width of vortex generator
x	coordinate along the centerline of model surface
x^*	normalized streamwise distance, x/δ
α	angle of incidence of vortex generator
δ	incoming boundary-layer thickness
y	coordinate in spanwise direction
y^*	normalized spanwise distance, y/δ
z	vertical distance from the surface

References

1. Wang, Y.; Liu, D.; Xu, X.; Li, G. Investigation of Reynolds number effects on aerodynamic characteristics of a transport aircraft. *Aerospace* **2021**, *8*, 177. [CrossRef]
2. Ashill, P.R.; Fulker, J.L.; Hackett, K.C. A reviews of recent developments in flow control. *Aeronaut. J.* **2005**, *109*, 205–232. [CrossRef]
3. Lin, J.C. Review of research on low-profile vortex generators to control boundary-layer separation. *Prog. Aerosp. Sci.* **2002**, *38*, 389–420. [CrossRef]
4. Lin, J.C.; Robinson, S.K.; Mcghee, R.J.; Valarezo, W.O. Separation control on high-lift airfoils via micro-vortex generators. *J. Aircr.* **1994**, *31*, 1317–1323. [CrossRef]
5. Lee, S.; Loth, E. Effect of Mach number on flow past microramps. *AIAA J.* **2011**, *49*, 97–110. [CrossRef]
6. Gaqeik, M.; Nies, J.; Klioutchnikov, I.; Oliver, H. Pressure wave damping in transonic airfoil flow by means of micro vortex generators. *Aerosp. Sci. Technol.* **2018**, *81*, 65–77. [CrossRef]
7. Titchener, N.; Babinsky, H. A review of the use of vortex generators for mitigating shock-induced separation. *Shock Waves* **2015**, *25*, 473–494. [CrossRef]
8. Bur, R.; Coponet, D.; Carpels, Y. Separation control by vortex generator devices in a transonic channel flow. *Shock Waves* **2009**, *19*, 521–530. [CrossRef]
9. Panaras, A.G.; Lu, F.K. Micro-vortex generators for shock wave/boundary layer interactions. *Prog. Aerosp. Sci.* **2015**, *74*, 16–47. [CrossRef]
10. Lee, S.; Loth, E. Impact of ramped vanes on normal shock boundary-layer interaction. *AIAA J.* **2012**, *50*, 2069–2079. [CrossRef]

11. Su, K.C.; Chung, K.M.; Isaev, S. Separation control for a transonic convex-corner flow using ramp-type vortex generators. *Int. J. Aerosp. Eng.* **2022**, *2022*, 4048490. [CrossRef]
12. Singh, N.K. Numerical simulation of flow behind vortex generators. *J. Appl. Fluid Mech.* **2019**, *12*, 1047–1061. [CrossRef]
13. Lu, F.K.; Li, Q.; Liu, C. Microvortex generators in high-speed flow. *Prog. Aerosp. Sci.* **2012**, *53*, 30–45. [CrossRef]
14. Baydar, E.; Lu, F.K.; Slater, J.W. Vortex generators in a two-dimensional external-compression supersonic inlet. *J. Prop. Power* **2018**, *34*, 521–538. [CrossRef]
15. Pearcey, H.H. Shock-induced separation and its prevention by design and boundary layer control. In *Boundary Layer and Flow Control: Its Principles and Application*; Pergamon Press: Oxford, UK, 1961; Volume 2, pp. 1166–1344.
16. Chung, K.C.; Su, K.C.; Chang, K.C. The effect of vortex generators on shock-induced boundary layer separation in a transonic convex-corner flow. *Aerospace* **2021**, *8*, 157. [CrossRef]
17. Chung, K.M. Unsteadiness of transonic convex-corner flows. *Exp. Fluids* **2004**, *37*, 917–922. [CrossRef]
18. Chung, K.M.; Huang, Y.X.; Lin, C.Y.; Wu, Y.T. Surface pressure measurements on a forebody using pressure-sensitive paint. *J. Aeronaut. Astronaut. Aviat.* **2021**, *53*, 369–374.
19. Chung, K.M.; Huang, Y.X. Global visualization of compressible swept convex-corner flow using pressure-sensitive paint. *Aerospace* **2021**, *8*, 106. [CrossRef]
20. Running, C.L.; Juliano, T.J. Global measurements of hypersonic shock-wave/boundary-layer interactions with pressure-sensitive paint. *Exp. Fluids* **2021**, *62*, 91. [CrossRef]
21. Wei, C.; Zuo, C.; Liao, X.; Li, G.; Jiao, L.; Peng, D.; Liang, L. Simultaneous pressure and displacement measurement on helicopter rotor blades using a binocular stereophotogrammetry PSP system. *Aerospace* **2022**, *9*, 292. [CrossRef]
22. Bell, J.H.; Schairer, E.T.; Hand, L.A.; Mehta, R.D. Surface pressure measurements using luminescent coatings. *Annu. Rev. Fluid Mech.* **2001**, *33*, 155–206. [CrossRef]
23. Huang, C.Y.; Lin, Y.F.; Huang, Y.X.; Chung, K.M. Pressure-sensitive paint measurements with temperature correction on the wing of AGARD-B under transonic flow conditions. *Meas. Sci. Technol.* **2021**, *32*, 094001. [CrossRef]